Research Article | Vol. 30, No. 14 / 4 Jul 2022 / Optics Express 25410

Optics EXPRESS

Terahertz difference-frequency-generation quantum cascade lasers on silicon with wire grid current injectors

JAE HYUN KIM,[1] WOLFHARD OBERHAUSEN,[2] SEUNGYONG JUNG,[1] JIAMING XU,[1] JIALIN MEI,[1] JEREMY D. KIRCH,[3] LUKE J. MAWST,[3] DAN BOTEZ,[3] AND MIKHAIL A. BELKIN[1,2,*]

[1] Department of Electrical and Computer Engineering, The University of Texas at Austin, Austin, Texas 78712, USA
[2] Walter Schottky Institute, Technical University of Munich, Garching 85748, Germany
[3] Department of Electrical and Computer Engineering, The University of Wisconsin-Madison, Madison, Wisconsin 53706, USA
[*] mikhail.belkin@wsi.tum.de

Abstract: We propose the concept and experimentally verify the operation of terahertz quantum cascade laser sources based on intra-cavity Cherenkov difference-frequency generation on a silicon substrate with the current injection layer configured as a metal wire grid. Such a current injector configuration enables high transmission of TM-polarized terahertz radiation into the silicon substrate while simultaneously providing a low-resistivity metal contact for current injection.

© 2022 Optica Publishing Group under the terms of the Optica Open Access Publishing Agreement

1. Introduction

Compact electrically-pumped narrow-linewidth coherent sources of terahertz (THz) radiation operating in the spectral range from 1 THz to 6 THz are highly desired for various applications such as biological and medical sciences, security, atmospheric science, environmental monitoring, and astronomy [1–4]. THz quantum cascade lasers (QCLs) are currently the only electrically-pumped semiconductor lasers operating in the 1-6 THz spectral range with a milliwatt-level power output. However, these devices still require cooling for operation [5–8]. To achieve room-temperature operation, THz QCL sources based on intra-cavity Cherenkov difference-frequency generation (DFG) in dual-wavelength mid-infrared (mid-IR, $\lambda \approx 3$-20 µm) QCLs, referred to as THz DFG-QCLs, have been proposed and developed [5,9–11]. A particular feature of THz DFG-QCLs is their ability to provide widely-tunable THz output with a tuning range from 1.2 to 5.9 THz demonstrated from a single THz DFG-QCL chip in Ref. [12].

The active regions of THz DFG-QCLs are designed so as to provide both optical gain for the mid-IR pumps as well as a giant second-order intersubband nonlinear susceptibility $\chi^{(2)}$ for THz DFG in the same laser cavity [13,14]. High THz absorption in the mid-IR laser waveguide prevents efficient extraction of THz radiation in edge-emitting devices [13,14]. To improve the THz outcoupling efficiency and to enable broadly-tunable THz output, THz DFG-QCLs with the Cherenkov phase matching scheme in which THz radiation is emitted from the laser active region into the device substrate were developed [5,9,15]. The schematic of these devices is as shown in Fig. 1(a). To enable Cherenkov DFG emission, the epilayer of the THz DFG-QCL needs to be optically coupled to a substrate with a THz refractive index (n_{sub}) larger than the mid-IR group index of the laser waveguide ($n_g \approx 3.3$-3.4 for InGaAs/AlInAs/InP QCLs) [15]. Traditionally, this is achieved by growing QCLs on semi-insulating (SI) InP substrates which have sufficiently high refractive index, see Fig. 1(b). However, SI InP substrates have significant THz absorption and strong refractive index dispersion that results in a beam steering in widely-tunable THz

#454780 https://doi.org/10.1364/OE.454780
Journal © 2022 Received 20 Apr 2022; revised 27 May 2022; accepted 1 Jun 2022; published 29 Jun 2022

DFG-QCLs [12,16,17]. It has recently been shown that the THz power output of THz DFG-QCLs can be improved dramatically if the SI InP substrates is substituted with float-zone high-resistivity (FZ HR) silicon (Si) substrate that has significantly lower absorption at THz frequencies and nearly-constant refractive index across the entire THz range as shown in Fig. 1(b) [16].

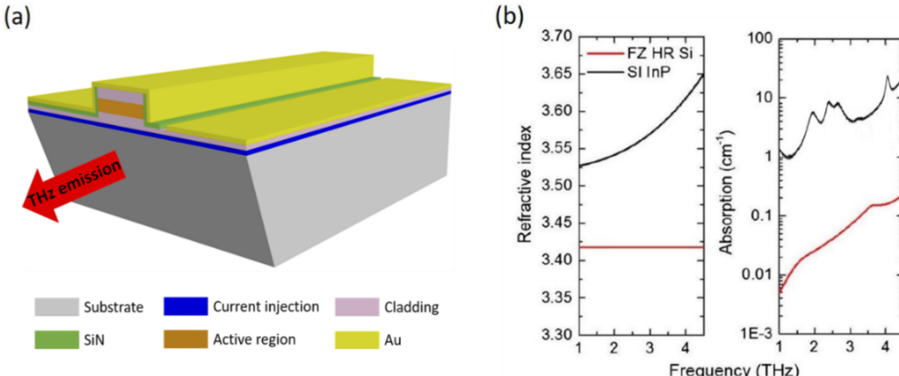

Fig. 1. (a) A schematic of ridge-waveguide Cherenkov THz DFG-QCLs. (b) Refractive indices (left panel) and absorption coefficients (right panel) of SI InP (black, higher values) and FZ HR Si (red, lower values) in the THz range. The data is taken from Ref. [16] and Ref. [17].

Since the substrate material for Cherenkov THz DFG-QCLs is semi-insulating, current injection into the laser needs to be provided laterally through the use of a current injection layer, shown in Fig. 1(a). When designing this layer, a balance must be struck between the requirements of low series resistance for current injection and low THz absorption losses for Cherenkov THz radiation extraction into the substrate. Traditionally, 100-to-200-nm-thick InGaAs layers with n-doping of approximately 1×10^{18} cm^{-3} are used in Cherenkov THz DFG-QCLs [10,12,15,16,18–20]. Their THz absorption in such layers varies from 10% to 50% of THz radiation depending on the frequency and the current-extraction-layer configuration with lower transmission values at lower THz frequencies [18]. The sheet resistance of such layers is in the range of 70-140 Ω/□ which translates into 1-5 of Ohms of series resistance for the current injection layer in individual devices, depending on the waveguide length and the distance to the metal side contact(s) on one or both sides of the laser ridge [18,19]. Given typical operating currents of 1-2 A and typical active region bias voltages of 10-15 V of individual DFG-QCL devices, such values of series resistance are considered acceptable for THz DFG-QCLs [5,9,10,11].

Future THz coherent output-power scaling in DFG-QCLs may be achieved by using DFG-QCL phase-locked laser arrays [21]. In that case, however, the pump current is significantly higher and the current-injection-layer path length is significantly longer compared to those in a single DFG-QCL device. In the first approximation, one may consider that both the current and the injection-layer path length scale with the number of QCL devices in the array. Given typical operating currents and bias voltages of individual DFG-QCL devices given above, the current injection layer, based on doped semiconductor layers, presents a significant limitation for the DFG-QCL array performance.

Here we propose and experimentally verify a concept of a metal-based current injection layer for the THz DFG-QCL configured as wire grid injector (WGI), a configuration inspired by that of a wire grid polarizer [22]. Such a current-injection-layer configuration allows one to simultaneously provide nearly arbitrarily low series resistance for current injection, while maintaining high transmission of THz radiation into the substrate. The WGI injection layer consists of an array of metal lines with sub-wavelength width in the direction perpendicular

Optics EXPRESS

to the orientation of the laser ridge as shown in Fig. 2(a). Since THz radiation generated in DFG-QCLs is TM-polarized, the WGI current injection pattern is nearly transparent for THz radiation transmission into the substrate.

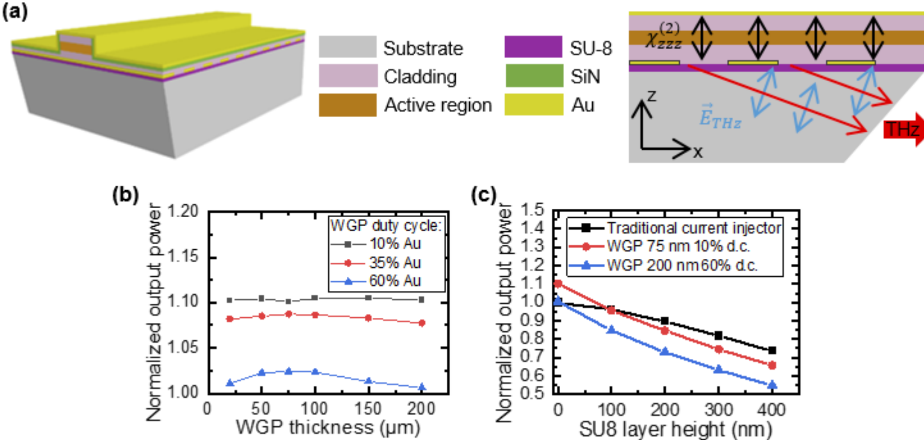

Fig. 2. (a) (left) Schematic illustration of Cherenkov THz DFG-QCLs on a FZ HR silicon substrate with the WGI current injector; (right)THz generation process, direction of the nonlinear polarization oscillations due to intersubband DFG process, and the polarization of the emitted THz radiation [5,13–15]. (b) Ratio of THz power output into the FZ HR silicon substrate of the device with a WGI injection and an identical device with a traditional current injector made of 200nm of InGaAs layer n-doped to 1×10^{18} cm^{-3}. The simulations assume direct device bonding to silicon (no SU-8 layer), DFG frequency of 3 THz, and a WGI period of 10 μm. The data is shown for the WGI injectors with different gold layer thicknesses and different WGI duty cycles. (c) Dependence of the THz DFG power output into the FZ HR silicon substrate on the SU-8 layer thickness for the THz DFG-QCLs with the traditional current injector layer made of 200nm of InGaAs layer n-doped to 1×10^{18} cm^{-3} and selected WGI current-injector configurations.

2. Simulation of wire-grid-injector THz extraction

The schematic of the THz DFG-QCL with the WGI current injection layer on a silicon substrate is shown in Fig. 2(a). The device configuration is similar to that of a Cherenkov THz DFG-QCLs on silicon [16], with the exception that the metal WGI current injector is used instead of a doped-semiconductor injector. To verify the concept of the WGI current injection scheme, we performed two-dimensional (slab-waveguide) electromagnetic simulations with COMSOL Multiphysics and compared the amount of THz radiation emitted into the substrate for the THz DFG-QCLs, using a traditional doped-semiconductor current injection layer, with the metal WGI current injection layer. In the simulations, a 600-nm-thick top gold contact layer is assumed to be placed on top of a 1 mm long DFG-QCL waveguide structure. We assumed a typical waveguide structure of THz DFG-QCLs designed for high-power pulsed operation: a 200-nm-thick plasma-enhanced upper cladding layer (InP, Si: 3.0×10^{18} cm^{-3}), a 4-μm-thick low-doped upper cladding layer (InP, Si: 1.2×10^{16} cm^{-3}), a 400-nm-thick upper mode confinement layer that may be used to fabricate a distributed feedback (DFB) grating ($In_{0.53}Ga_{0.47}As$, Si: 1.0×10^{16} cm^{-3}), a 4.6 μm-thick active region ($In_{0.53}Ga_{0.47}As$ and $Al_{0.48}In_{0.52}As$, average doping of 3.6×10^{16} cm^{-3}), a 200-nm-thick lower mode confinement layer ($In_{0.53}Ga_{0.47}As$, Si: 1.0×10^{16} cm^{-3}), and a 4-μm-thick lower cladding layer (InP, Si: 1.2×10^{16} cm^{-3}) followed by the current injection layer. The WGI current injection layer is created by etching grooves into the lower cladding layer and afterwards filling these with gold. The height of the gold layer is chosen to be equal to the groove depth,

in order to planarize the structure. We compared the performance of the devices with the WGI current injection layer with that of the devices having traditional 200 nm thick InGaAs layers with n-doping of 1×10^{18} cm^{-3} positioned right below the bottom surface of the lower cladding layer. The simulations further assume that THz DFG-QCL devices are transfer-printed on top of a float-zone (FZ) high-resistivity (HR) silicon substrate for THz DFG radiation extraction using a layer of SU-8 epoxy (Kayaku Advanced Materials, Inc.) as an adhesive, similar to that used in Ref. [16].

The DFG process was modelled by introducing a polarization source in the active region imitating the 3 THz DFG polarization wave propagating towards the outcoupling facet of the laser. The mid-IR group index and the THz refractive index of SU-8 layer are assumed to be 3.37 and $1.7 + i \times 0.029$, respectively [23]. Figures 2(b,c) shows the comparison of the computed THz power emission into the FZ HR silicon substrate per unit length of the device for the case of the WGI injector and a traditional 200-nm-thick InGaAs injector with n-doping of 1×10^{18} cm^{-3} for several different WGI-injector thicknesses and duty cycles and for different thicknesses of the SU-8 adhesive. Figure 2(b) plots the ratio of THz emission from a device with a WPG injector with a period of 10 µm directly bonded to the FZ HR silicon substrate (no SU-8 adhesive) with an identical device having a traditional 200-nm-thick InGaAs current injector with n-doping of 1×10^{18} cm^{-3} directly bonded to the FZ HR silicon substrate. The ratio is plotted for different gold-layer thickness and duty cycles of the WGI current injector. We note that a WGI period of 10 µm is sufficiently small to avoid diffraction of 3 THz radiation. Figure 2(c) shows how the THz DFG emission into the substrate decreases as the SU-8 adhesive thickness increases for the case of devices with the WGI and transitional current injectors. The reduction of THz power emitted into the substrate for thicker SU-8 adhesive layers is primarily due to its low refractive index of the SU-8 epoxy, which results in evanescent coupling of THz radiation into the substrate. We note that one can achieve high-quality bonding with the SU-8 epoxy as thick as 100 nm [16].

The data in Fig. 2(c) indicates that, assuming that a sufficiently thin SU-8 bonding layer is used, THz DFG-QCLs on FZ HR Si with WGI are expected to have similar or better THz outcoupling efficiency compared to the devices with traditional semiconductor-based injectors, while providing significantly lower series resistance. Specifically, as mentioned above, the traditionally-used 200 nm thick InGaAs current injection layer with n-doping of 1×10^{18} cm^{-3} has a sheet resistance of approximately 70 Ω/□. In comparison, a 75 nm thick WGI with a duty cycle of 10% is expected to have a sheet resistance of 3.3 Ω/□ [24].

3. Experimental demonstration and discussion

To verify the feasibility of operation of the Cherenkov THz DFG-QCLs on FZ HR Si with WGI current injection layers experimentally, the THz DFG-QCL structure was grown on a 350-µm-thick semi-insulating InP substrate. The growth started with a 200-nm-thick $In_{0.53}Ga_{0.47}As$ etch-stop layer (Si: 1.0×10^{16} cm^{-3}), followed by a 20-nm-thick InP contact layer (Si: 5.0×10^{18} cm^{-3}), a 4.0-µm-thick InP cladding layer (Si: 1.2×10^{16} cm^{-3}), and a 200-nm-thick $In_{0.53}Ga_{0.47}As$ waveguide layer (Si: 1.0×10^{16} cm^{-3}). Then, two 31-repetition stacks of $In_{0.53}Ga_{0.47}As/In_{0.52}Al_{0.48}As$ bound-to-continuum active regions optimized for THz DFG nonlinearity with a 300-nm-thick InP spacer layer (Si: 1.0×10^{16} cm^{-3}) between them were grown. The layer sequence of one period of the bottom active region is **43**/20/**11**/55/**11**/53/**11**/48/**15**/37/**15**/36/**16**/33/**18**/31/**20**/29/**24**/29/**26**/27/**30**/27, and that of the top active region is **39**/22/**10**/59/**10**/57/**11**/53/**12**/43/**14**/39/**15**/37/**16**/35/**19**/33/**23**/31/**25**/31/**29**/30, where the layer thickness is in Angstroms, and the bold and underlined characters denote the $In_{0.52}Al_{0.48}As$ layers and doped (Si: 1.6×10^{17} cm^{-3}) layers, respectively. On top of the active region, a 400-nm-thick $In_{0.53}Ga_{0.47}As$ waveguide layer (Si: 1.0×10^{16} cm^{-3}), a 4.0-µm-thick InP upper cladding layer (Si: 1.2×10^{16} cm^{-3}), a 200-nm-thick InP upper plasmon layer (Si: 3.0×10^{18} cm^{-3}), and a 20-nm-thick InP top contact layer (Si: 2.0×10^{19} cm^{-3}) were grown.

Optics EXPRESS

The key device processing steps are shown in Fig. 3. For processing, an approximately 1.2 cm by 1.2 cm piece was cleaved from the QCL wafer. Double-channel ridge waveguides with ridge widths of 16 µm were defined by optical lithography and dry etching. The sidewalls of the laser ridges were insulated with a 500-nm-thick SiN layer. Following the top metal contact deposition, the processed wafer was thermocompressively bonded, epi-side down, to a metal-coated n-doped InP host wafer as shown in Fig. 3(a). The n-doped InP host wafer was used to support the waveguide structure during the following fabrication steps and it served as a contact to the top of the laser ridge waveguide. The SI InP substrate of the bonded QCL piece was then removed by selective etching. Following the substrate removal, a 1-mm-wide WGI pattern was defined on the backside of the laser ridge. First, we used optical lithography and wet-etching to define approximately 200-nm-deep grooves in the 200-nm-thick $In_{0.53}Ga_{0.47}As$ etch-stop layer. These grooves were then filled with metal for creating the WGI injector. To that end, the photoresist mask remained on the device and a metal layer (Ti/Au ≈ 20 nm/180 nm) was deposited on top by e-beam evaporation. The photoresist mask was then used in a lift-off process to create a WGI injector with the metal layers positioned in the grooves etched in the $In_{0.53}Ga_{0.47}As$ layer. Afterwards, the back side of the n-doped InP substrate was metallized to form one of the device contacts. The processed wafer, shown schematically in Fig. 3(b), was then cleaved into single laser devices with the cavity length of 4 mm, and these devices were spin-coated with a 400-nm-thick SU-8 layer. We note that here we used a rather thick SU-8 layer for the proof-of-concept demonstration to simplify processing and make it less sensitive to sample surface contamination. The laser facet and the wire-bonding area were covered by the Crystalbond glue (Ted Pella, Inc., Crystalbond 509) before SU-8 spin coating to protect them from SU-8 deposition. Finally, a 3-mm-long FZ HR Si wafer piece with the front facet polished at an angle of 15° was manually bonded to the device and the assembly was baked on a hot plate at 180 °C for the SU-8 layer to cure. The length of a FZ HR Si prism was slightly shorter than the length of the laser to enable wire bonding for current injection as shown in Fig. 3(c).

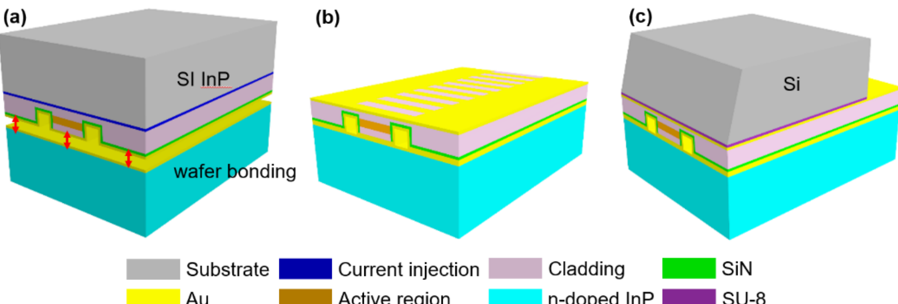

Fig. 3. The key fabrication steps. (a) Episide-down thermo-compression metal-metal wafer bonding of the fully-processed THz DFG-QCLs on their native SI InP substrate onto an n-doped InP 'host' substrate. (b) Following the selective native SI InP substrate removal, the gold WGI current injector as well as gold contact pads are defined on the exposed device epilayer. (c) Wafer bonding of the WGI device with a FZ HR silicon substrate using a SU-8 adhesive layer.

The scanning electron microscopy image of the back section of the processed THz DFG-QCL with WGI current injector and with the attached FZ HR Si prism is shown in Fig. 4(a). Figure 4(b) is a close-up image that shows the details of the WGI current injector including the metal stripes in the etched semiconductor grooves and the un-etched semiconductor regions. The WGI metal wires do not fill the entire etched grooves in the semiconductor, which is due to the underetching the photoresist mask formed during the isotropic wet-etching process that was mentioned earlier. Since the same photoresist was used as a lift-off mask for the WGI fabrication, the underetching

Optics EXPRESS

resulted in the incomplete filling of the semiconductor grooves with metal. The problem of underetching may be addressed in the future by employing dry etching techniques. The image shows that the period and the duty cycle of the WGI are 10 µm and 60%, respectively. The width of the un-etched regions is 2 µm and the width of the etched regions without metal deposition is 1 µm. The thickness of the metal lines in the WGI injection were measured to be 210 nm, while the etch depth of the semiconductor grooves was measured to be 200 nm. This results in a slightly uneven device surface. This imperfection can, however, be accommodated by the SU-8 adhesive layer that was used for the Si-prism bonding.

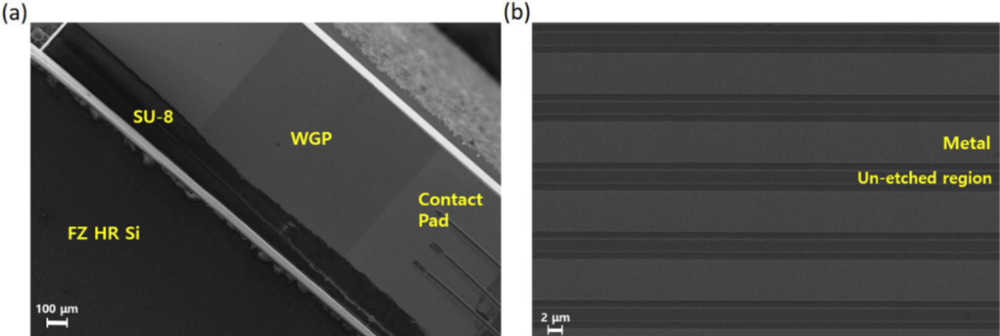

Fig. 4. Scanning electron microscopy images of the THz DFG-QCL device with a WGI current injector and the FZ HR Si prism bonded to the front section of the device using an SU-8 adhesive layer. (a) Top view of the device. The WGI section, SU-8 adhesive layer, FZ HR Si substrate, and metal contact pad connected to the WGI metal wires for current injection are indicated with yellow text. (b) Magnified image of a WGI section. Metal stripes and un-etched semiconductor regions are indicated with yellow text.

For the measurement, devices with a ridge width of 16 µm and a cavity length of 4 mm were indium-soldered to a copper block with the n-doped InP substrate facing the block and successively wire bonded. The laser device was then mounted into a dual-grating external cavity setup, which is reported in Ref. [25], that was used to select two mid-IR pump frequencies for THz DFG. Devices were operated with 50 ns current pulses at 20 kHz repetition rate at room temperature. Reference 4-mm-long and 16-µm-wide ridge-waveguide Cherenkov DFG-QCL on SI InP substrate devices were also fabricated from the same QCL wafer and tested to evaluate the performance of the WGI devices.

Figure 5(a) shows the mid-IR and THz emission spectra measured from the THz DFG-QCL with the WGI current injector and a silicon prism. Two mid-IR pumps were selected at 978 cm^{-1} and 1079 cm^{-1}, and the THz frequency was measured to be 101 cm^{-1} (3.0 THz), in agreement with the difference between two mid-IR pump frequencies. Figure 5(b) shows the light output-current characteristics for the mid-IR pumps of the WGI device. The mid-IR pump powers were measured using a thermopile detector with two parabolic mirrors and corrected for the estimated 70% collection efficiency of our setup. The measured current-voltage characteristics of the WGI device and a reference SI InP device are also shown as a black solid line and a black dashed line, respectively. The voltage of the WGI device is considerably lower than that of the reference devices, as expected. The sheet resistance in the WPG structure is estimated to be around 0.2 Ω/□, which results in the expected series resistance of the 1-mm-wide WGI injector of around 0.025 Ω in our 4-mm-long devices. The remaining series resistance of the WGI devices was attributed to contact resistance.

The THz peak power and the mid-IR-to-THz conversion efficiency, which is traditionally defined for THz DFG-QCLs as the ratio of the THz peak power to the product of the two mid-IR pump powers [5,9–15,17–19,25,26], as a function of current are shown in Fig. 5(c) for the WGI

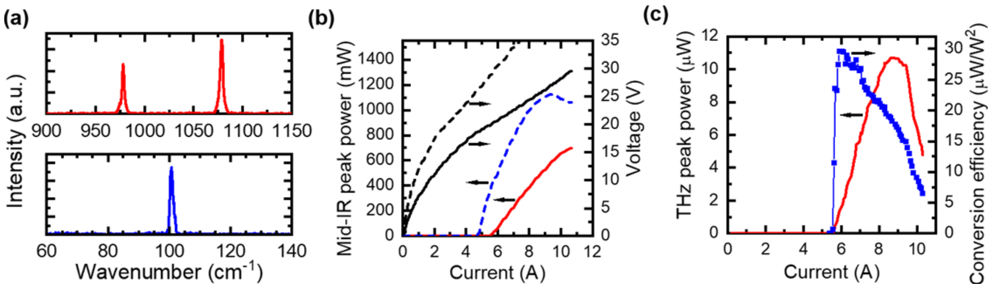

Fig. 5. Performance of a 16-μm-wide and 4-mm-long ridge-waveguide THz DFG-QCL on a silicon substrate with a WGI current injector. The device was tested in pulsed mode at room temperature in a dual-grating external cavity setup. (a) Emission spectra of the mid-IR pumps (top) and THz DFG (bottom). (b) Voltage (solid black line) and the peak power outputs (dashed blue and solid red lines) of the two mid-IR pumps vs current. The dashed blue line and the solid red line refer to the power output of the short-wavelength and long-wavelength mid-IR pumps, respectively. The black dashed line refers to the current-voltage characteristic of the reference InP device of the same dimensions. (c) THz peak power output (red solid line) and the mid-IR-to-THz conversion efficiency (blue squares) of the device using the WGI injection scheme and a silicon prism as a function of pump current.

device. A calibrated liquid helium cooled Si bolometer with two parabolic mirrors was used to measure the THz power and no collection-efficiency correction were made. The maximum THz peak power of the WGI device is 10.7 μW and the mid-IR-to-THz conversion efficiency at this THz power is 18.8 $\mu W/W^2$. This conversion efficiency is 1.8 times higher than that of the reference SI InP device of the same length. As shown in Fig. 2(c), we expect a factor of 2 of further improvement in the THz power for the WGI injectors with lower duty cycles and silicon prism being bonded with thin SU-8 adhesive. Further improvements in the THz output are expected in devices with complete filling of the semiconductor grooves with metal and with the silicon prism covering the entire length of the laser. With these future improvements, DFG-QCL devices with WGI current injectors on FZ HR silicon are expected to reach THz extraction efficiency levels similar to that of devices with doped InGaAs current injectors on FZ HR silicon demonstrated in Ref. [16], while having significantly lower series resistance.

4. Conclusion

We have presented a concept for a metal current injector configured as a WGI for the operation of Cherenkov THz DFG-QCLs. The WGI current-injector design provides simultaneously low series resistance for current transport to the device and high transparency for the TM-polarized THz radiation. We have confirmed the feasibility of the new current-injector operation with proof-of-concept devices that have shown a factor of 1.8 higher mid-IR-to-THz conversion efficiency compared to reference Cherenkov THz DFG-QCL on SI InP devices at 3.0 THz.

Funding. Army Research Office (W911NF-16-C-0128); ConTex (UTA17-001106); Deutsche Forschungsgemeinschaft (442667270); Intraband, LLC; Kwanjeong Educational Foundation (12AmB06G).

Acknowledgements. The work of the University of Texas at Austin group was supported by the Army Research Office and the ConTex program. The work of the Technical University of Munich group was supported by the Deutsche Forschungsgemeinschaft. Funding was provided to the University of Wisconsin–Madison group by Intraband, LLC, with which D. Botez and L. J. Mawst have significant financial interests. J.H.K acknowledges support from the Kwanjeong Educational Foundation (KEF).

Disclosures. D. Botez and L. J. Mawst have significant financial interests with Intraband, LLC (I).

Data availability. Data underlying the results presented in this paper are not publicly available at this time but may be obtained from the authors upon reasonable request.

Optics EXPRESS

References

1. M. Tonouchi, "Cutting-edge terahertz technology," Nat. Photonics **1**(2), 97–105 (2007).
2. P. F. Taday, I. V. Bradley, D. D. Arnone, and M. Pepper, "Using Terahertz pulse spectroscopy to study the crystalline structure of a drug: a case study of the polymorphs of ranitidine hydrochloride," J. Pharm. Sci. **92**(4), 831–838 (2003).
3. M.C. Kemp, P.F. Taday, B.E. Cole, J.A. Cluff, A.J. Fitzgerald, and W.R. Tribe, "Security applications of terahertz technology," Terahertz Mil. Secur. Appl. **5070**, 44–52 (2003).
4. P. H. Siegel, "Terahertz technology," IEEE Trans. Microw. Theory Tech. **50**(3), 910–928 (2002).
5. M. A. Belkin and F. Capasso, "New frontiers in quantum cascade lasers: high performance room temperature terahertz sources," Phys. Scr. **90**(11), 118002 (2015).
6. A. Khalatpour, A. K. Paulsen, C. Deimert, Z. R. Wasilewski, and Q. Hu, "High-power portable terahertz laser systems," Nat. Photonics **15**(1), 16–20 (2021).
7. G. Liang, T. Liu, and Q. J. Wang, "Recent Developments of Terahertz Quantum Cascade Lasers," IEEE J. Sel. Top. Quantum Electron. **23**, 1200118 (2017).
8. L. Bosco, M. Franckié, G. Scalari, M. Beck, A. Wacker, and J. Faist, "Thermoelectrically cooled THz quantum cascade laser operating up to 210 K," Appl. Phys. Lett. **115**(1), 010601 (2019).
9. Q. Lu and M. Razeghi, "Recent Advances in Room Temperature, High-Power Terahertz Quantum Cascade Laser Sources Based on Difference-Frequency Generation," Photonics **3**(3), 42 (2016).
10. M. Razeghi, Q. Y. Lu, N. Bandyopadhyay, W. Zhou, D. Heydari, Y. Bai, and S. Slivken, "Quantum cascade lasers: from tool to product," Opt. Express **23**(7), 8462 (2015).
11. M. Razeghi, "Terahertz emitters at Center for Quantum Devices: recent advances and future trends," Proc. SPIE **10383**, 1038305 (2017).
12. Y. Jiang, K. Vijayraghavan, S. Jung, F. Demmerle, G. Boehm, M. C. Amann, and M. A. Belkin, "External cavity terahertz quantum cascade laser sources based on intra-cavity frequency mixing with 1.2–5.9 THz tuning range," J. Opt. **16**(9), 094002 (2014).
13. M. A. Belkin, F. Capasso, A. Belyanin, D. L. Sivco, A. Y. Cho, D. C. Oakley, C. J. Vineis, and G. W. Turner, "Terahertz quantum-cascade-laser source based on intracavity difference-frequency generation," Nat. Photonics **1**(5), 288–292 (2007).
14. M. A. Belkin, F. Capasso, F. Xie, A. Belyanin, M. Fischer, A. Wittmann, and J. Faist, "Room temperature terahertz quantum cascade laser source based on intracavity difference-frequency generation," Appl. Phys. Lett. **92**(20), 201101 (2008).
15. K. Vijayraghavan, R. W. Adams, A. Vizbaras, M. Jang, C. Grasse, G. Boehm, M. C. Amann, and M. A. Belkin, "Terahertz sources based on Čerenkov difference-frequency generation in quantum cascade lasers," Appl. Phys. Lett. **100**(25), 251104 (2012).
16. S. Jung, J. H. Kim, Y. Jiang, K. Vijayraghavan, and M. A. Belkin, "Terahertz difference-frequency quantum cascade laser sources on silicon," Optica **4**(1), 38–43 (2017).
17. L. N. Alyabyeva, E. S. Zhukova, M. A. Belkin, and B. P. Gorshunov, "Dielectric properties of semi-insulating Fe-doped InP in the terahertz spectral region," Sci. Rep. **7**(1), 7360 (2017).
18. K. Vijayraghavan, Y. Jiang, M. Jang, A. Jiang, K. Choutagunta, A. Vizbaras, F. Demmerle, G. Boehm, M. C. Amann, and M. A. Belkin, "Broadly tunable terahertz generation in mid-infrared quantum cascade lasers," Nat. Commun. **4**(1), 2021 (2013).
19. Q. Y. Lu, N. Bandyopadhyay, S. Slivken, Y. Bai, and M. Razeghi, "Room temperature terahertz quantum cascade laser sources with 215 μ W output power through epilayer-down mounting," Appl. Phys. Lett. **103**(1), 011101 (2013).
20. Q. Y. Lu, S. Slivken, N. Bandyopadhyay, Y. Bai, and M. Razeghi, "Widely tunable room temperature semiconductor terahertz source," Appl. Phys. Lett. **105**(20), 201102 (2014).
21. J. D. Kirch, C.-C. Chang, C. Boyle, L. J. Mawst, D. Lindberg III, T. Earles, and D. Botez, "5.5 W near-diffraction-limited power from resonant leaky-wave coupled phase-locked arrays of quantum cascade lasers," Appl. Phys. Lett. **106**(6), 061113 (2015).
22. P. Yeh, "A new optical model for wire grid polarizers," Opt. Commun. **26**(3), 289–292 (1978).
23. M. Naftaly and R. E. Miles, "Terahertz Time-Domain Spectroscopy for Material Characterization," Proc. IEEE **95**(8), 1658–1665 (2007).
24. T. H. Gilani and D. Rabchuk, "Electrical resistivity of gold thin film as a function of film thickness," Canadian J. Phys. **96**(3), 272–274 (2018).
25. Y. Jiang, K. Vijayraghavan, S. Jung, A. Jiang, J. H. Kim, F. Demmerle, G. Boehm, M. C. Amann, and M. A. Belkin, "Spectroscopic Study of Terahertz Generation in Mid-Infrared Quantum Cascade Lasers," Sci. Rep. **6**(1), 21169 (2016).
26. Q. Y. Lu, N. Bandyopadhyay, S. Slivken, Y. Bai, and M. Razeghi, "Continuous operation of a monolithic semiconductor terahertz source at room temperature," Appl. Phys. Lett. **104**(22), 221105 (2014).

129.187.254.46 2025-03-18 10:45:(